AGU PUBLICATIONS

Water Resources Research

RESEARCH ARTICLE
10.1002/2017WR020726

Key Points:
- How river evolution works out the floodplain structure
- Long term evolution of alluvial systems
- Metrics to compare synthetically generated and observed meandering planforms

Supporting Information:
- Supporting Information S1
- Table S1–S3

Correspondence to:
M. Bogoni,
manuel.bogoni@dicea.unipd.it

Citation:
Bogoni, M., M. Putti, and S. Lanzoni (2017), Modeling meander morphodynamics over self-formed heterogeneous floodplains, *Water Resour. Res.*, *53*, 5137–5157, doi:10.1002/2017WR020726.

Received 9 MAR 2017
Accepted 28 MAY 2017
Accepted article online 2 JUN 2017
Published online 27 JUN 2017

Modeling meander morphodynamics over self-formed heterogeneous floodplains

Manuel Bogoni[1], Mario Putti[2], and Stefano Lanzoni[1]

[1]Department of Civil, Environmental and Architectural Engineering, University of Padova, Padova, Italy, [2]Department of Mathematics, University of Padova, Padova, Italy

Abstract This work addresses the signatures embedded in the planform geometry of meandering rivers consequent to the formation of floodplain heterogeneities as the river bends migrate. Two geomorphic features are specifically considered: scroll bars produced by lateral accretion of point bars at convex banks and oxbow lake fills consequent to neck cutoffs. The sedimentary architecture of these geomorphic units depends on the type and amount of sediment, and controls bank erodibility as the river impinges on them, favoring or contrasting the river migration. The geometry of numerically generated planforms obtained for different scenarios of floodplain heterogeneity is compared to that of natural meandering paths. Half meander metrics and spatial distribution of channel curvatures are used to disclose the complexity embedded in meandering geometry. Fourier Analysis, Principal Component Analysis, Singular Spectrum Analysis and Multivariate Singular Spectrum Analysis are used to emphasize the subtle but crucial differences which may emerge between apparently similar configurations. A closer similarity between observed and simulated planforms is attained when fully coupling flow and sediment dynamics (fully-coupled models) and when considering self-formed heterogeneities that are less erodible than the surrounding floodplain.

Plain Language Summary This work concerns the modeling of the long-term evolution of meandering rivers flowinf above self-formed floodplains, i.e., floodplains that have been modified by the river itself. The erosion and deposition processes at the banks due to the flow field into the river introduce heterogeneity in the surface composition and thus in the spatial distribution of the erosional resistance, such that the river may experience faster or slower migration rates depending on its previous configurations (i.e., the migration history). Present results show that the heterogeneity in floodplain composition associated with the formation of geomorphic units (i.e., scroll bars and oxbow lakes) and the choice of a reliable flow field model to drive channel migration are two fundamental ingredients for reproducing correctly the long-term morphodynamics of alluvial meanders. Floodplain heterogeneity was found to affect both the temporal and spatial distributions of meander metrics, eventually leading to a closer statistical similarity between simulated and natural planform shapes.

1. Introduction

River patterns are the result of the mutual feedbacks between channel morphodynamics, floodplain destruction by bank erosion, and floodplain formation [*Kleinhans*, 2010]. A number of processes drive floodplain genesis, among which the most common are vertical accretion during overbank floods, lateral point bar accretion as meandering rivers migrate, and braided channel accretion [*Nanson and Croke*, 1992]. Sediment sorting along river bars and across the floodplain, and vegetation encroachment, also contribute to determine the sedimentary architecture of the fluvial landscape, promoting the formation of natural levees that, in turn, control natural flooding frequency and overbank sedimentation [*Howard*, 1996; *Kleinhans*, 2010]. Eventually, the sediment removed from the floodplain is swept back to the channel [*Dunne et al.*, 1998; *Aalto et al.*, 2008; *Swanson et al.*, 2008; *Lauer and Parker*, 2008].

The sedimentary architecture of a floodplain is strictly linked to the pattern of rivers therein [*Nanson and Croke*, 1992], even though physiographic constraints such as the valley width [*Howard*, 1996; *Nicoll and Hickin*, 2010] and tectonic shift [*Schumm*, 1986] can also be important. Channel-forming discharge, sediment

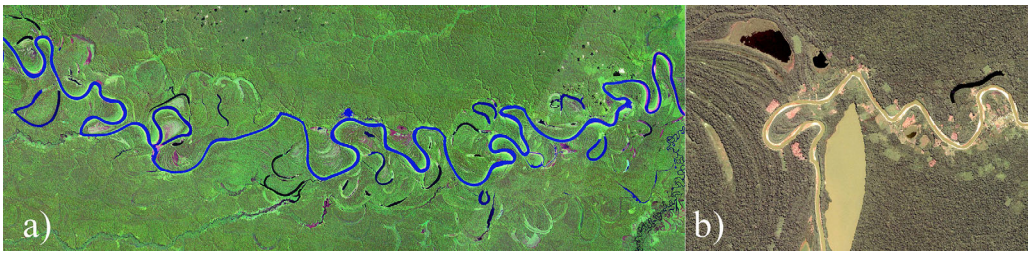

Figure 1. Examples of two scenarios concerning heterogeneous floodplains at different spatial scales. a) Landsat detail of the Jurua River floodplain, Brazil (source: USGS EarthExplorer). Actual size of the frame area is about 85 × 31 km. River flows from left to right. Many features typical of meandering channel floodplains are visible: skewed meanders, point bars at the inner side of bends, scroll bars, ancient river paths, incipient forming cutoffs, recent cutoffs still flooded, and older oxbow lakes covered by vegetation of the Amazon rainforest. b) Long-term migration of the Rio Tamay (Peru) leads the channel path into a part of the floodplain previously reworked by the Ucayali River, consisting of ridge-and-swale scroll bars and of a partially filled oxbow lake. Actual size of frame area is about 4.5×3.5 km. Rio Tamai flows from right to left (source: Google Earth Pro).

supply, and bank strength are the fundamental factors that determine the morphology of alluvial rivers [*Schumm*, 1985; *Ferguson*, 1987]. At the channel belt scale channel patterns are observed to change from straight, to meandering, to braiding (multiple thalwegs) with increasing flow intensity and decreasing bank strength [*Makaske*, 2001]. The amount and the type of sediment supply matter as well, influencing bank strength and sedimentation/erosion processes [*Ferguson*, 1987]. At the floodplain scale, higher-order channel patterns (e.g., anastomosing) can be observed [*Makaske*, 2001].

Depending on the sedimentary environment, on the formative processes, and on the flow intensity, three main classes of floodplains can be distinguished on the basis of the specific stream power ω at bankfull [*Nanson and Croke*, 1992]: high-energy noncohesive ($\omega > 300$ W m^{-2}), medium-energy noncohesive ($\omega = 10-300$ W m^{-2}), and low-energy cohesive ($\omega < 10$ W m^{-2}). In the present contribution we are specifically interested in medium-energy noncohesive floodplains that are reworked by the lateral migration of a meandering river (Figure 1). Fine sediment (fine sands, silt, and clay) accumulates across these floodplains mainly as a consequence of over-bank flooding (vertical overbank accretion), while sand and gravel contribute to point bar deposits. In the case of scroll-patterned surfaces, these deposits consist of a ridge-and-swale sequence, yielding an heterolithic stratification of interbedded sand and mud deposits with lateral accretion surfaces [*Nanson*, 1980; *Day et al*., 2008; *van de Lageweg et al*., 2014]. Crevasse splay through levee breaches, over-bank spilling of tie and tributary channels, floodplain channels, organic-reach backswamp deposits, and fine-grained fills of abandoned channels and oxbow lakes further contribute to design the heterogeneous structure of the floodplain [*Howard*, 1996; *Slingerland and Smith*, 2004; *Gautier et al*., 2007; *Day et al*., 2008; *Swanson et al*., 2008; *David et al*., 2016].

The balance between floodplain formation and destruction determines the width of the migrating channel and, consequently, the formation of a given fluvial pattern. The seminal work of *Blondeaux and Seminara* [1985] shows that a meandering pattern eventually forms as a result of bend instability, whereby small perturbations of an initially straight channel alignment grow, driven by erosion at concave banks and deposition at convex banks [*Seminara*, 2006]. Depending on the half-width to depth ratio β of the channel, single meanders can be either upstream skewed and migrate downstream (sub-resonant regime, $\beta < \beta_r$) or downstream skewed and migrate upstream (super-resonant regime, $\beta > \beta_r$) [*Seminara et al*., 2001; *Lanzoni et al*., 2006]. Resonance ($\beta = \beta_r$) describes the intrinsic response of a straight channel, consisting of a sequence of alternate stationary bars, that would not develop spontaneously, but can be excited in the presence of an external forcing provided by channel curvature.

The effects of floodplain heterogeneity on meandering dynamics have been addresses by various researchers. Meandering patterns throughout complex floodplain deposits have been found to differ from those typical of homogeneous floodplain deposits [*Hudson and Kesel*, 2000; *Lazarus and Constantine*, 2013]. In their pioneering works, *Howard* [1996] and *Sun et al*. [1996] coupled together the flow field model derived by *Johannesson and Parker* [1989] and the bank erosion law of *Ikeda et al*. [1981] to reproduce the geometric forms of individual meanders observed in natural sedimentary environments with different erodibility (point bars, floodplain deposits, and oxbow lake fills). More recently, *Güneralp and Rhoads* [2011] and *Motta et al*. [2012b] published two similar works dealing with the influence of a priori generated distribution of

floodplain heterogeneities on rates and patterns of meander migration. Both studies conclude that adopting a relatively simple flow field model, and prescribing a priori the erodibility distribution across the floodplain, allow to generate bend complexity and planform irregularity similar to those observed in alluvial rivers, both visually and in their spectra of planform curvature. In the last years, various studies have been also devoted to examine the role of the vegetation cover on floodplain erodibility [e.g., *Perucca et al*., 2006; *Solari et al*., 2016; *van Oorschot et al*., 2016; *Zen et al*., 2016].

In the present work we investigate the role played in river meandering by floodplain heterogeneities that form as a consequence of lateral point bar accretion and filling of abandoned oxbow lakes. These self-formed heterogeneities are shown to significantly reflect on the statistics of planform meandering shapes. Differently from *Howard* [1996] and *Sun et al*. [1996], a more refined fully-coupled hydrodynamic and morphodynamic model [*Zolezzi and Seminara*, 2001, hereinafter ZS] is implemented to compute the curvature-driven flow field that drives bend migration. The widely-used uncoupled approach of *Ikeda et al*. [1981] (IPS) is here considered simply for comparison purposes, given its extensive use in previous analyses [*Perucca et al*., 2005; *Güneralp and Rhoads*, 2011; *Motta et al*., 2012a, 2012b; *Schwenk et al*., 2015; *Schuurman et al*., 2016].

The aim of the study is twofold: i) evaluating the mutual interactions between a self-formed heterogeneous floodplain and the meandering river which flows within it, and ii) measuring objectively the structure of numerically generated patterns through a suite of statistical tools and metrics, and ultimately comparing the modeled planforms against observed river paths. Indeed, a spatial point-by-point comparison of model results and natural rivers is not feasible owing to the uncertainties in initial and boundary conditions, the simplifications embodied by the models, and the presence of empirical constants that need to be calibrated [*Kleinhans*, 2010]. An extensive database of numerically generated meander planforms is thus created by varying the relevant parameters within physically plausible ranges. Three different statistical tools are used to evaluate quantitatively the influence of the adopted mathematical models and their accuracy in reproducing natural planforms, namely the Singular Spectrum Analysis (SSA) and its Multivariate extension (MSSA), the Fourier Analysis (FA), and the Principal Component Analysis (PCA).

We find that floodplain heterogeneities generated by meandering river migration can have a significant impact on river planform geometry. This emerges when comparing different paths through suitable half meander metrics, and is reasonably captured by a relatively simplified mathematical model that fully couples the flow field and the bed evolution equation, tracking the positions of heterogeneous sedimentary units originating from sediment sorting.

2. Material and Methods

The present mathematical and numerical frameworks build upon a fully-coupled hydrodynamic and morphodynamic model that, for a constant (in time and space) floodplain erodibility, has been shown to reproduce correctly the large variety of meandering bend forms (simple bends, compound bends and multiple loops) observed in alluvial rivers [e.g., *Camporeale et al*., 2005; *Lanzoni et al*., 2006; *Lanzoni and Seminara*, 2006; *Frascati and Lanzoni*, 2009]. It consists of a migration model for the meandering channel axis (section 2.1), a model for updating the floodplain structure as the channel migrates (section 2.2), and a morphodynamic model for evaluating the curvature-driven flow that controls outer bank erosion (section 2.3). Starting from a initially straight, slightly and randomly perturbed configuration, the model simulates the long-term planform evolution of a meandering river across an initially homogeneous floodplain (hereafter denoted as pristine floodplain), made by fine sediment deposits accumulated by over-bank flooding or resulting from the lateral accretion of nonscrolled point bars. The resulting planforms are analyzed through the statistical and spectral tools described in section 2.4.

The floodplain is assumed to have a constant slope. It is referred to a Cartesian coordinate system (x^*, y^*, z^*), where z^* coincides with the vertical pointing upward. The channel, lying on the floodplain plane x^*-y^*, is described through the orthogonal curvilinear coordinate system (s^*, n^*, z^*), where s^* is the streamwise coordinate of the channel axis, and n^* is the horizontal axis locally normal to the plane s^*-z^*. Hereafter the superscript * denotes dimensional quantities. By definition, the curvature of the channel axis is $C^*=1/R^*=-\partial\theta/\partial s^*$, where R^* is the local curvature radius and θ is the local angle that the tangent to the channel axis forms with the x^*-direction.

The meandering channel has a width $2B_0^*$, a characteristic grain size d_s^* (e.g., d_{50}^*), and conveys a constant bankfull discharge $Q^*=2B_0^*D_0^*U_0^*$, where D_0^* and U_0^* are the mean depth and cross-sectionally averaged velocity of an equivalent straight channel with slope S_0 carrying the same discharge Q^*.

2.1. Long-Term River Migration

The long-term migration of meandering rivers is driven by the complex interplay of erosion at the outer bank and deposition at the inner bank. Among others, the relevant factors are the type of bank failure, the composition of the banks and of the slumped block material, and the vegetation cover properties, all controlling the bank strength required to limit the width to depth ratio and, consequently, to impede the transition to braiding. Erosion and deposition processes usually occur at different time scales [*Asahi et al.*, 2013]. However, over the long time scale characterizing meandering planform dynamics and floodplain reworking, an overall balance is usually attained, and a nearly constant width is maintained as the channel sinuosity evolves [*Parker et al.*, 2011]. Normal distributions of width oscillations correlated with channel curvature can arise as a result of the temporary cross-section widening near the bend apex (bank pull) caused by outer bank erosion during floods [*Frascati and Lanzoni*, 2013; *Wickert et al.*, 2013]. In many cases, the subtle interplay of bank pull and bank push due to point bar progradation drives the formation of a typical ridge-and-swale point bar topography [*Eke et al.*, 2014; *van de Lageweg et al.*, 2014; *Schuurman et al.*, 2016].

The river migration across the floodplain produces a local displacement $\xi_n^*(s^*,t^*)$ along the direction n^* normal to the channel axis. The corresponding local migration rate is:

$$\zeta^*(s^*,t^*)=\frac{d\xi_n^*}{dt^*} \tag{1}$$

where t^* denotes time. In general, ζ^* depends on the bank strength and on the stream characteristics. For constant channel width, it can be expressed through the relation proposed by *Ikeda et al.* [1981] that, in dimensionless form, reads:

$$\zeta=E\,U_b \tag{2}$$

where $\zeta=\zeta^*/U_0^*$ and E is a dimensionless long-term erosion coefficient. The dimensionless excess near-bank velocity, $U_b=U_b^*/U_0^*$, driving bank erosion, is given by the difference between the longitudinal velocity $U|_{n=1}$ at the outer bank ($n=n^*/B_0^*=1$) and the longitudinal velocity $U|_{n=-1}$ at the inner bank ($n=n^*/B_0^*=-1$). Both ζ and U_b are functions of the longitudinal dimensionless coordinate $s=s^*/B_0^*$.

The problem outlined above is solved numerically by discretizing the river centerline through a polyline made by N points $P_i(x_i,y_i)$, with $(x_i,y_i)=(x_i^*,y_i^*)/B_0^*$. The differential equation (1) is solved numerically trough finite differences. At each dimensionless time step $t^{k+1}=t^k+\Delta t^k$ (with $t=t^*U_0^*/B_0^*$), the migration of the ith node in the direction n normal to s is computed through a time marching procedure of the form [*Crosato*, 1990]:

$$x_i^{k+1}=x_i^k-\Delta t_i^k\,\frac{\zeta_i^k+\zeta_i^{k-1}}{2}\sin\theta_i^k, \tag{3}$$

$$y_i^{k+1}=y_i^k+\Delta t_i^k\,\frac{\zeta_i^k+\zeta_i^{k-1}}{2}\cos\theta_i^k, \tag{4}$$

where $x_i^{k+1}=x_i(t^{k+1})$, $y_i^{k+1}=y_i(t^{k+1})$, $\zeta_i^k=E_i^k\,U_{bi}^k$. The value θ_i^k of the local angle of deviation with respect to the longitudinal direction is computed by backward and forward averaging [*Lanzoni and Seminara*, 2006]:

$$\theta_i^k=\frac{1}{2}\left(\arctan\frac{y_{i+1}^k-y_i^k}{x_{i+1}^k-x_i^k}+\arctan\frac{y_i^k-y_{i-1}^k}{x_i^k-x_{i-1}^k}\right) \tag{5}$$

This angle is used to compute the local value of the dimensionless curvature $\mathcal{C}_i^k$ by discretizing the relation $\mathcal{C}=-(1/v_0)\partial\theta/\partial s$ as [*Frascati and Lanzoni*, 2013]:

$$\mathcal{C}_i^k=-\frac{1}{v_0}\,\frac{\theta_{i+1}^k-\theta_{i-1}^k}{2\Delta s_i^k} \tag{6}$$

where Δs_i^k is the dimensionless distance between two consecutive points of the axis, $v_0=B_0^*/R_0^*$ is the curvature ratio, with R_0^* taken equal to the minimum value of R^* along the channel reach. The possible numerical

anomalies arising from the curvature computation are filtered out by using a Savitzky-Golay smoothing filter [*Orfanidis*, 1995; *Frascati and Lanzoni*, 2009; *Motta et al*., 2012a; *Schwenk et al*., 2015]. The time step size Δt_i^k is controlled by requiring that:

$$\Delta t_i^k \leq \alpha \left(\frac{\Delta s_i^k}{E_i^k U_{bi}^k} \right)_{\max} \tag{7}$$

where α is a parameter defining the threshold between stable and unstable computations, to be chosen empirically ($\alpha \sim 10^{-2}$) on the basis of a balance between computational effort and accuracy of the numerical solution [*Crosato*, 1990; *Lanzoni and Seminara*, 2006]. Since the deformation experienced by the channel axis at each time step leads to continuous variations of the point spacing, the mesh is periodically re-built to maintain quasi-uniformity of the node spacings, adding or removing nodes to maintain the value of Δs_i^k within the range 2/3 and 4/3.

Cutoffs are another typical product of channel shifting that needs to be accounted for when considering long-term meandering evolution. They remove older, well developed meanders, limiting the planform complexity of the channel and, consequently, ensuring the establishment of statistically stationary evolving planforms [*Camporeale et al*., 2005; *Frascati and Lanzoni*, 2010]. In addition, abandoned loops create accommodation space for sediment storage, forming fine sediment fills that contribute to the overall sediment balance of the channel-floodplain system [*Gagliano and Howard*, 1984; *Gay et al*., 1998; *Hooke*, 2004; *Constantine et al*., 2010; *Grenfell et al*., 2012]. Oxbow lake geometry is thus a story-holder of the river migration dynamics [*Schwenk et al*., 2015] and a control factor for the future evolution of the system [*Camporeale et al*., 2005]. In the present modeling framework, we model only the formation of neck cutoffs, whereby the upstream and downstream portions of a bend loop approach each other and eventually intersect. As a first approximation, chute cutoffs are not considered.

Following *Howard and Knutson* [1984] and *Sun et al*. [1996], the presence of potential neck cutoffs is detected by controlling the dimensionless distance between a given point P_i and the nearby points P_{i+r} located sufficiently downstream (e.g., $r \geq 8$). This control is made through the algorithm developed by *Camporeale et al*. [2005], which improves the computational efficiency of the model. When the computed Cartesian distance between nodes P_i and P_{i+r} is lower than a threshold value, say $\Delta s_r = 2.2$, all the points P_{i+j}, $j = 1, r-1$ are removed from the computational grid, defining a new oxbow lake (Figure 2). A few nodes upstream of P_i and downstream of P_{i+r} (e.g., P_{i-q}, P_{i+r+q}, $q = 1, 2, 3$) are also removed to prevent the formation of a high-curvature river reach [*Frascati and Lanzoni*, 2009] that, in nature, is unlikely to persist owing to the rapid smoothing action of the current and to the propagation along the river of the geometric disturbances generated by the cutoff event [*Hooke*, 1995; *Camporeale et al*., 2008].

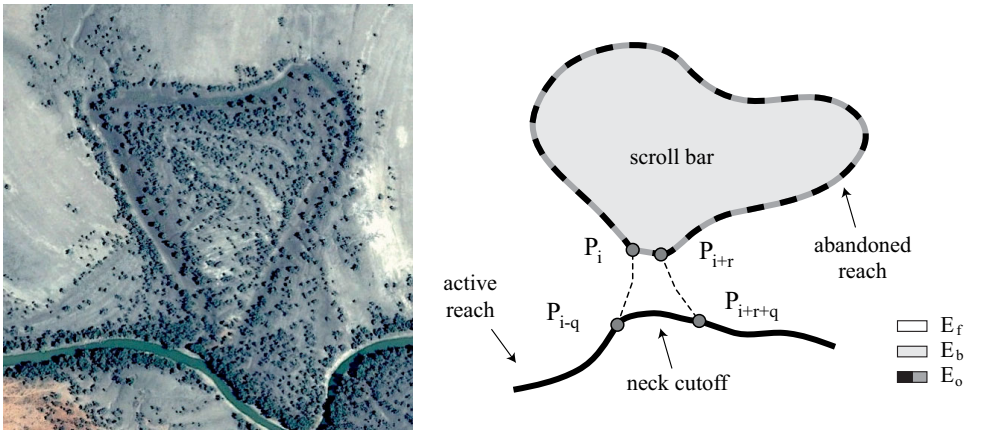

Figure 2. (a) Example of a neck cutoff occurred in the Darling River, Australia (31° 33′ S 143° 30′ E, source: Google Earth Pro); (b) numerical modeling of a neck cutoff, with the formation of an abandoned oxbow lake and a point bar complex. Symbols are as follows: r is the number of the points that are considered to check the occurrence of an incipient neck cutoff; q is the number of points removed to avoid the establishment of a high-curvature river reach after a cutoff; E_f, E_b, and E_o are the erodibility coefficients assigned to the pristine floodplain, the point bar complex and the abandoned oxbow lake, respectively.

2.2. Floodplain Features

The bank strength of alluvial rivers generally depends on many factors: soil properties, selective deposition and consolidation processes, groundwater dynamics [*Han and Endreny*, 2014], and distribution of riparian vegetation [*Perucca et al*., 2007; *Motta et al*., 2012a, 2012b; *Wickert et al*., 2013]. In order to mimic the heterogeneities in bank strength caused by different sediment deposits and vegetation encroachment, the floodplain surface is, as a first approximation, schematized by three possible geomorphic units with different values of the erosion coefficient E (Figure 2).

The first geomorphic unit is the pristine undisturbed floodplain, with erosion coefficient E_f. It corresponds to an already existing homogeneous floodplain, consisting of fine sediment deposits not yet reworked by the river migration. Its genesis can be related to lateral accretion by nonscrolled point bars or oblique accretion under moderate energy conditions, or to repeated overbank floods, crevasse channels and splays in low energy environments [*Nanson and Croke*, 1992].

The second kind of geomorphic units corresponds to abandoned oxbow lakes, having erosion coefficient E_o. It mimics the channel fills that form during the transitional phase of active channel abandonment and the disconnected phase starting after the complete abandonment due to a neck cutoff. The sedimentary architecture of these fills depends on the type and amount of sediment filling [*Constantine et al*., 2010]. In particular, it is determined by the initial formation of plug bars at the oxbow channel entrances, followed by a progressive shallowing and narrowing during the channel abandonment, and the formation of laminated fill facies (composed of silt and/or clay) after the abandonment [*Toonen et al*., 2012]. Wash load delivered during floods and, in some cases, sediment-laden flow conveyed by tie channels [*Rowland et al*., 2005] are mainly responsible for oxbow filling. This process may last for many decades, depending on the rate of sediment supply, and eventually can lead to the formation of sediment plugs that slow meander migration [*Hudson and Kesel*, 2000].

Finally, the third geomorphic unit corresponds to the scroll bar environment, with erosion coefficient E_b. It mimics the scroll-patterned area bounded by the inner bank of an oxbow lake, characterized by a ridge-and-swale sequence with coarse-grained sediment accumulating on ridges and finer sediments (silt and clay) depositing in the upper parts [*Nanson*, 1980] caused by the temporary flow expansions due to bank pull [*van de Lageweg et al*., 2014]. Additional erosion-resistant plugs inhibiting lateral channel migration are associated to the fine-grained concave scroll bar-shaped deposits that form on the most distal parts of point bars (the counter point bars defined by *Smith et al*. [2009]). The interaction of vegetation cover (Figure 2a) with the local topography and hydrological conditions [*Zen et al*., 2016] adds further complexity to the scroll bar units. Usually, vegetation contributes to reinforce the ridge-and-swale configuration [*Swanson et al*., 2008], favoring the bar-floodplain conversion [*Schuurman et al*., 2016; *van Oorschot et al*., 2016].

All the erosion coefficients are kept constant over time in order to maintain the modeling framework at the lowest possible level of complexity. Moreover, on the long time scales over which the river planform evolves, we assume that the formation of the sedimentary architectures associated with scroll bars and oxbow lakes is much faster than the time required by the river to intersect them. Temporal variations caused, for instance, by soil compaction and vegetation dynamics are not considered. Incision of new channels, soil uplift and subsidence are not accounted for as well, assuming that the floodplain surface is infinitely large and keeps its elevation constant over time. Finally, possible changes in the hydrological regime and flow unsteadiness associated with flood waves are neglected.

The spatial variability of soil strength ensuing from the meandering dynamics is accounted for as follows. The erosion coefficients associated with the heterogeneous geomorphic units (oxbow lakes and scroll bars) are switched to the prescribed values as soon as they are identified geometrically, i.e., after a neck cutoff. All the heterogeneous geomorphic units that progressively form as the river migrates are saved as polygons formed by the mesh nodes delimiting the unit area (Figure 3). As the generic node P_i of the active channel axis migrates laterally, the river may encounter three different environments during its lateral migration within the floodplain. The winding number algorithm of *Hormann and Agathos* [2001] is used to identify whether the current point lies within a presaved geomorphic unit and, hence, to choose the appropriate value of the local erosion coefficient.

2.3. The Flow Field Model

The flow in meandering channels is strongly dependent on the secondary helical flow that arises in a bend as a consequence of three mechanisms [*Bolla Pittaluga and Seminara*, 2011; *Frascati and Lanzoni*, 2013]: (i) the

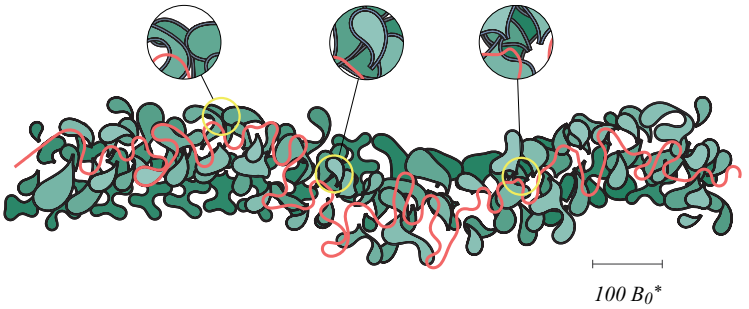

Figure 3. Example of a simulated planform dynamics, with the formation of oxbow lakes (gray stripes) and scroll bars (older are dark green, younger are light green).

metric effect which tends to accelerate the inner bank flow and retard the outer bank flow as a consequence of the lateral variation in longitudinal bed slope; (ii) the free vortex effect, due to centripetal acceleration, that determines an inward directed pressure gradient and a lateral free surface slope; and (iii) the topographic steering due to the bar-pool pattern. The resulting flow field is three-dimensional.

Nevertheless, for the purpose of long-term morphodynamics, a quasi-two dimensional approach can be pursued [*Zolezzi and Seminara*, 2001]. The three dimensional equations governing mass and momentum conservation, written in curvilinear coordinates, are averaged over the flow depth and a suitable parametrization is introduced to preserve the memory of the centrifugally and topographically induced secondary flow circulations. The resulting set of depth-averaged equations are then coupled with the Exner sediment balance equation, and closed by means of a prescribed flow resistance relationship and a sediment transport law. An analytical solution of the problem can be obtained taking advantage of the small values usually attained by parameters like the curvature ratio [*Zolezzi and Seminara*, 2001] and the normalized width oscillations [*Frascati and Lanzoni*, 2013]. The governing equations are linearized and the dependent variables are expanded in Fourier series. Eventually, a system of four fourth-order ordinary differential equations (ODEs) is obtained for each of the *m*th Fourier modes. The resulting excess near-bank velocity needed to compute the migration rate takes the functional form:

$$U_b^* = U_0^* F[\nu_0, \beta, C_f, \tau_*, R_p, \mathcal{C}, \int_0^s \mathcal{C}(\xi)\, e^{\lambda_{mj}(s-\xi)}\, d\xi] \tag{8}$$

where, in addition to the curvature ratio ν_0 and the half width to depth ratio $\beta = B_0^*/D_0^*$, the relevant parameters are the dimensionless grain size $d_s = d_s^*/D_0^*$, the Shields number $\tau_* = C_f U_0^{*2}/\Delta g d_s^*$, the particle Reynolds number $R_p = \sqrt{g\Delta d_s^{*3}}/\nu$. Here g is the gravity acceleration, $\Delta = (\rho_s - \rho)/\rho$ is the submerged specific gravity of the sediment ($\rho_s \simeq 2650$ kg/m^3, $\rho = 1000$ kg/m^3), C_f is the friction coefficient, and ν the kinematic viscosity of the water. The four characteristic exponents λ_{mj} $(m = 0, \infty; j = 1, 4)$, which result by solving for each Fourier mode the above mentioned fourth-order ODEs, are crucial to determine the morphodynamic behaviour of meandering channels. Indeed they control, through the convolution integrals, whether the flow and the bed topography at a given position s are affected by the river reach located upstream (downstream influence, sub-resonant regime) or downstream (upstream influence, super-resonant regime) [*Zolezzi and Seminara*, 2001; *Lanzoni and Seminara*, 2006]. It is important to observe that a super-resonant behaviour cannot emerge when using a flow field model not coupled with the sediment conservation equation in which the transverse bed slope has to be assigned empirically (e.g., IPS model). In this case, moreover, exaggeratedly upstream skewed meanders are often predicted, as values of wavelengths and sinuosities are in general too high (see results below).

Further details about the derivation, performances and limitations inherent to the modeling approach can be found in *Zolezzi and Seminara* [2001], *Lanzoni and Seminara* [2006], and *Frascati and Lanzoni* [2013]. Here, we simply recall that the four dimensionless parameters β, d_s, τ_*, and R_p fully characterize the steady flow and the sediment transport conditions that establish in the river. Under dominant bedload conditions the sediment transport intensity Φ is computed through the formula of *Parker* [1990], while the total load predictor of *Engelund and Hansen* [1967] is used when suspended load prevails, the thresholds being given by the empirical relations proposed by *Browlie* [1981] and *Van Rijn* [1984a]. The particle Reynolds number R_p is also used to establish whether the river bed is flat or dune-covered [*Van Rijn*, 1984b] when computing the friction coefficient C_f through the *Engelund and Hansen* [1967] method.

As the river planform evolves, the total channel length and the bed slope change over time. As a consequence, suitable relations must be imposed in order to keep consistent steady flow and sediment transport conditions. Assuming a constant discharge and a temporally constant floodplain gradient, the relevant physical parameters between two time steps k and $k+1$ are updated as follows:

$$\frac{\beta^{k+1}}{\beta^k} = \left(\frac{C_f^k}{C_f^{k+1}}\right)^{1/3} \left(\frac{\sigma_T^k}{\sigma_T^{k+1}}\right)^{1/3} \tag{9}$$

$$\frac{\tau_*^{k+1}}{\tau_*^k} = \left(\frac{C_f^k}{C_f^{k+1}}\right)^{-1/3} \left(\frac{\sigma_T^k}{\sigma_T^{k+1}}\right)^{2/3} \tag{10}$$

$$\frac{d_s^{k+1}}{d_s^k} = \left(\frac{C_f^k}{C_f^{k+1}}\right)^{1/3} \left(\frac{\sigma_T^k}{\sigma_T^{k+1}}\right)^{1/3} \tag{11}$$

where σ_T is the river sinuosity, defined as the ratio of the intrinsic length L^*, computed along the channel centerline, to the Cartesian length l_x^* obtained by projecting the river axis along the direction of the floodplain gradient.

2.4. Statistical Tools

No general methods are available to reveal objectively similarities and differences among nonlinear patterns that vary both in time and space as river planforms. Spatial series of local curvatures [*Perucca et al.*, 2005] and time evolution of reach averaged quantities (e.g., mean wavelength, mean sinuosity) have been considered to synthesize the dynamic of the system [*Camporeale et al.*, 2005; *Frascati and Lanzoni*, 2010]. However, the significance of these measures in summarizing the intrinsic features of the whole system dynamics, and hence its state, is not known a priori. Several morphometric variables referring to individual meander or to reach averaged properties may indeed act as state parameters [*Howard and Hemberger*, 1991; *Frascati and Lanzoni*, 2009]. In the present contribution we analyze spatial distributions of full meander curvatures through Fourier Analysis (FA) and Singular Spectrum Analysis (SSA), and apply Multivariate Singular Spectrum Analysis (MSSA) to half meander metrics. Finally, we use a suite of statistical parameters to compare globally, through Principal Component Analysis (PCA), the geometrical features of meander planforms.

The Fourier Analysis is a linear technique that applies to stationary signals and has been widely adopted in the study of local curvature distribution associated with meandering planforms [*Marani et al.*, 2002; *Güneralp and Rhoads*, 2011; *Motta et al.*, 2012b]. The power spectrum is used to identify the most important components of the curvature distributions, i.e., the modes that mostly contribute to the reproduction of the overall signal. The comparison between the dominant components helps to disclose objectively possible affinities/differences between the considered signals.

Spatial (and temporal) variability of river patterns however calls for a statistical methodology able to manage nonstationary signals. For this reason, in addition to FA, we use SSA and its multivariate extension, MSSA. They are in fact powerful and flexible techniques that allow for identifying simultaneously the main trends and the oscillatory behaviour of a given series (either spatial or temporal), and to reveal and separate random noise from the significant signal [*Vautard and Ghil*, 1989]. Within the context of environmental applications, SSA has been used to extract information from noisy climatic and geomagnetic time series [*Ghil et al.*, 2002; *Serita et al.*, 2005]. SSA analysis proceeds by evaluating the principal components of a time-lagged covariance matrix using a lag-window of size M (see supporting information). This procedure is extended through MSSA to a multivariate input signal (e.g., the set of half meander metrics) composed of L dimensions and previously normalized by PCA [*Ghil et al.*, 2002]. Because of the splitting along the various components, SSA leads to a possible separation between fundamental components of the signal and higher-order noise, thus it is an indicator of the complexity of the signal structure. In particular, the faster the spectrum decays, the larger the separation between the fundamental signal and noise, and thus the less the signal scattering. On the contrary, the larger the spectrum mildness (low slope), the higher the signal complexity due to the possible weight of higher-order noise.

The Principal Component Analysis is a technique already considered in the analysis of river planforms [*Howard and Hemberger*, 1991; *Frascati and Lanzoni*, 2009]. We applied it to a suite of morphometric parameters in order to characterize the river paths, either simulated or natural. Paths similarity can be objectively evaluated by looking at the variance distribution (the eigenvalues) along the principal directions (the eigenvectors) of the correlation matrix. This approach facilitates the identification of the differences that contribute the most to the formation of the deviations among signals coming from the various samples.

3. A Test Case: Two Versus Three Erodibility Environments

This test case is designed to allow a first quantitative evaluation of the interactions between the long-term evolution of meanders and floodplain heterogeneities (oxbow lakes and scroll bars) formed as a river migrates across an initially homogeneous floodplain (the pristine floodplain). The erosion coefficient E of the initial floodplain is set equal to $E_f = 10^{-8}$ [*Frascati and Lanzoni*, 2009]. This value has the same order of magnitude of that considered by *Sun et al*. [1996], and is intermediate between those used by *Motta et al*. [2012a] (10^{-9}) and *Constantine et al*. [2009] (10^{-7}). Referring to the sketch in Figure 2, six scenarios are investigated by accounting or excluding the effect of abandoned oxbow lakes and considering three different values of erosional resistance E_b for the scroll bar units: $E_b = E_f$, homogeneous scenario; $E_b = 3\,E_f$, softening scenario; $E_b = E_f/3$, hardening scenario. The erosion coefficient of oxbow lakes is set equal to either $E_o = E_f$ or $E_o = E_f/10$ since, in the long term, abandoned oxbows are likely to be filled by fine grained sediments forming less erodible plugs.

Table 1 summarizes the six investigated scenarios. The first case (H_{om}) consists of a floodplain which, in term of erodibility, is not modified by the river evolution. In other words, the river has no memory about its own past configurations. The second case (O_{xb}) considers the formation of oxbow lakes that, after their disconnection and infilling, have an erosional resistance larger (i.e., lower erodibility coefficient) than that of the pristine floodplain, while scroll bars are assumed not to alter significantly the floodplain erodibility. The third and the fourth cases (S_{oft} and $S_{oft}O_{xb}$) concern the formation of scroll bars which are more erodible than the surrounding floodplain, such that the river experiences a faster migration throughout them. Oxbow lake effects are either excluded (S_{oft}) or included ($S_{oft}O_{xb}$). These two scenarios might roughly correspond to a river which flows in a floodplain formed by fine sediment deposits (silt and clay) and transports coarser sediment which is deposited on the inner bend point bars during floods. The effect of the coarser material layers on scroll bar erodibility is assumed to dominate over the effect given by fine layers deposited during the falling stage of floods. Alternatively, the scenarios may be assumed to mimic a river dynamics which is faster than the time required by the strengthening actions due to soil compaction and vegetation encroachment. The fifth and the sixth cases (H_{ard} and $H_{ard}O_{xb}$) assume that scroll bars are less erodible than the surrounding floodplain, such that the river migrates more slowly when it flows across them. Also in this case, oxbow lake effects are excluded (H_{ard}) or included ($H_{ard}O_{xb}$). These two scenarios might roughly correspond to a river which flows through floodplain deposits formed by relatively coarse material and deposits mainly fine sediment on the point bars. The effect on erodibility due to the finer layers of the scroll bars is assumed to be stronger than the one due to the coarser layers. Alternatively, the

Table 1. Different Erosional Scenarios Considered in the Test Cases[a]

	Oxbow Lakes		Scroll Bars		L_h		A_h		σ_h	
Scenario	Case	E_o/E_f	Case	E_b/E_f	Mean	St.dev.	Mean	St.dev.	Mean	St.dev.
H_{om}	no	1	no	1	44.6	4.2	−0.14	0.03	1.79	0.11
O_{xb}	yes	1/10	no	1	21.5	1.1	0.07	0.04	1.23	0.02
S_{oft}	no	1	softening	3	41.5	4.2	−0.12	0.04	1.67	0.12
$S_{oft}O_{xb}$	yes	1/10	softening	3	20.5	1.1	0.06	0.05	1.26	0.03
H_{ard}	no	1	hardening	1/3	31.1	3.5	−0.06	0.04	1.47	0.11
$H_{ard}O_{xb}$	yes	1/10	hardening	1/3	21.6	1.1	0.01	0.04	1.19	0.03

[a]They account for the presence of oxbow lakes which are less erodible than the surrounding floodplain ($E_o < E_f$), or exclude this effect assuming that oxbow lakes are not distinguishable from the pristine floodplain ($E_o = E_f$). These two scenarios are then coupled with those assuming that scroll bars are more erodible ($E_b > E_f$), less erodible ($E_b < E_f$), and as erodible as the pristine floodplain ($E_b = E_f$). The mean and standard deviations of the half meander metrics L_h, A_h, and σ_h are evaluated after statistically-steady evolution of the planform configurations are attained.

scenarios may mimic the rapid formation of a vegetation cover that stabilizes the point bar, leading to a bank strengthening as the river impinges again on that area.

All runs started from the same initial morphologic configuration consisting in a homogeneous floodplain crossed by a straight channel, perturbed in the transverse direction with small random fluctuations, normally distributed with zero mean and standard deviation of 0.01 B_0^*. The initial dimensionless parameters in this test case are $\beta = 20$, $\tau^* = 0.7$, $d_s = 0.0005$, $R_p = 400$, which correspond to $2B_0^* = 175$ m, $D_0^* = 4.30$ m, $S_0 = 5.8 \times 10^{-4}$, and $d_s^* = 2.1$ mm (coarse sand). Assuming a Strickler coefficient equal to $K_s = 25$ m$^{1/3}$ s^{-1}, the uniform flow velocity, the discharge and the Froude number read, respectively:

$$U_0^* = K_s D_0^{*2/3} S_0^{1/2} = 1.59 \text{ m/s} \tag{12}$$

$$Q^* = 2B_0^* D_0^* U_0^* = 1190 \text{ m}^3/\text{s} \tag{13}$$

$$F_r = U_0^* / \sqrt{g D_0^*} = 0.245 \tag{14}$$

According to *Latrubesse* [2008], the considered river may be classified as a large river, being the discharge larger than 1000 m^3/s. Among the several approaches present in the literature to discriminate channel patterns, the discharge/slope approaches of *Leopold and Wolman* [1957] and *Lane* [1957] provide respectively $S_{\text{lim}} = 5.8 \times 10^{-4}$ and $S_{\text{lim}} = 1.2 \times 10^{-3}$ as the threshold that discriminates between braided rivers ($S > S_{\text{lim}}$) and meandering rivers ($S < S_{\text{lim}}$). The considered test case thus just equals the braided-meandering threshold of the first classification, whereas it is largely in the meander domain when considering the latter classification. The slope-Froude number approach of *Parker* [1976] gives $S_{\text{lim}} = 6.1 \times 10^{-3}$, thus confirming the meandering behaviour.

According to the empirical classifications of *Van den Berg* [1995] and *Makaske et al.* [2002], the value of the specific stream power, $\omega = \rho g U_0^* D_0^* S = 39$ W/m^2, suggests that the tested river likely lies in the domain of meandering rivers, with occurrence of scrolls and chutes. Indeed, the initial straight path is unstable and the river experiences an elongation due to the lateral growth of bends starting from the very first iterations.

Figure 4 shows the simulated migration history for the six different erodibility scenarios, after a time equal to 20 times the time t_{fc} at which the first cutoff occurs. The hardening scenarios whereby oxbow lakes and/or scroll bars are less erodible than the pristine floodplain (O_{xb}, H_{ard}, $S_{oft}O_{xb}$, $H_{ard}O_{xb}$) generates a wavy meander belt of width of about 100–120 B_0^*. The remaining two scenarios (the homogeneous case H_{om}, and the softening scenario without oxbow lakes S_{oft}) exhibit a meander belt that is nearly straight and has a width of about 180–200 B_0^*.

In order to characterize quantitatively the time evolution of the simulated landforms, we considered three half meander metrics (i.e., defined along reaches delimited by two consecutive inflection points of the channel axis). They are: the dimensionless half meander length L_h (scaled by B^*), the half meander sinuosity σ_h, and the half meander asymmetry A_h [*Howard and Hemberger*, 1991; *Frascati and Lanzoni*, 2009]:

$$\sigma_h = \frac{L_h}{l_h} \tag{15}$$

$$A_h = \frac{L_h^u - L_h^d}{L_h} \tag{16}$$

Here L_h and l_h are the intrinsic and Cartesian lengths between two inflection points, while L_h^u and L_h^d are the intrinsic lengths upstream and downstream of the point of maximum curvature $\mathcal{C}_{\text{max}}$ along the considered half meander. Note that A_h ranges in the interval (-1, 1) and determines whether the half meander is upstream skewed ($A_h < 0$), downstream skewed ($A_h > 0$), or symmetric ($A_h = 0$). The three metrics are averaged over the N_h half meanders forming the river path at the time t. Their temporal trends are plotted in Figure 5.

The river begins initially to elongate monotonically ($t < t_{fc}$, where t_{fc} is the time at which the first cutoff occurs), and the pristine floodplain area reworked by channel migration increases as well. The initial straight condition leads to an artificial regularity of the developing meander trains, which implies that adjacent meanders approach neck cutoffs nearly simultaneously [*Frascati and Lanzoni*, 2010]. After the first cutoff occurrence ($t > t_{fc}$), self-formed floodplain heterogeneities begin to affect the meander evolution process.

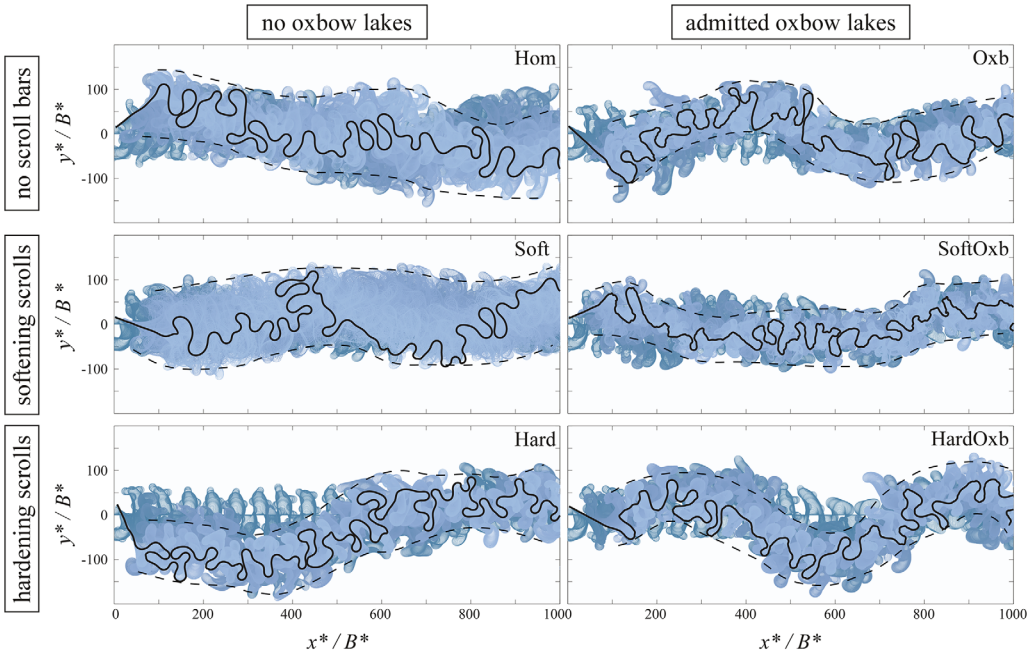

Figure 4. Migration history of the river planforms, simulated for the six scenarios defined in Table 1. The dimensionless parameters used for the initial straight configuration are $\beta = 20$, $\tau^* = 0.7$, $d_s = 0.0005$. Darker paths are older, while lighter paths are younger. Dashed lines mark qualitatively the active meander belt width.

The trajectory corresponding to the homogeneous case H_{om} separates from the others and deviations are more remarkable for L_h and σ_h. At a later stage of evolution ($t > t_{se}$) cutoffs remove older meanders, limiting the planform geometrical complexity and leading to a state of statistical stationary evolution (hereafter SSE). The time signals oscillate about nearly constant values. This condition is attained for t_{se} ranging from $\sim 2\, t_{fc}$ when considering less erodible oxbow lakes, to $\sim 4\, t_{fc}$ for softening scroll bars.

After SSE is established, in the absence of any heterogeneity (H_{om}) meanders tend to be upstream skewed. Assuming more erodible scroll bars (S_{oft}) produces upstream skewed, slightly shorter and less sinuous meanders. The presence of erosion resistant plugs associated with abandoned oxbows (O_{xb}) generally leads to definitely much shorter, less sinuous and downstream skewed meanders. The three scenarios including less erodible oxbow lakes (O_{xb}, $H_{ard}O_{xb}$, $S_{oft}O_{xb}$) exhibit minor differences from the statistical point of view. An intermediate behaviour is attained by excluding oxbow lake effects and assuming that scroll bars are less erodible than the pristine floodplain (see statistics in Table 1). Lastly it is noteworthy that all the results of Figures 4 and 5 are consistent with those of *Camporeale et al*. [2005], who observed that the width of meander belt is about 3.0 - 3.8 times the mean Cartesian wavelength l_f. Recalling that $l_f = 2\, L_h/\sigma_h$, and using the data in Table 1, the belt width falls in the range 2.8 - 4.0 times l_f.

4. Data and Results

This section describes the characteristics of the considered data sets concerning natural and numerically generated planforms, and the statistical and spectral analyses carried out on them. Different analyses are performed on half meander metrics (frequency distribution and MSSA) and spatial distributions of full meander curvature (FA and SSA). Finally, PCA is applied to a suite of variables describing the meander planforms, in order to compare globally the geometrical features of natural and simulated paths.

4.1. Natural and Simulated Planforms

The first data set consists of 52 natural planforms of meandering rivers, obtained from literature data or extracted from Landsat and Google Maps images, and selected in order to include paths from different continents and environments. The list is reported in the supporting information Table S2 and S3.

The second database groups the planforms generated numerically to cover a relatively wide range of natural-equivalent cases. It is built by considering 18 sets of initial dimensionless parameters, β, τ^*, d_s, and

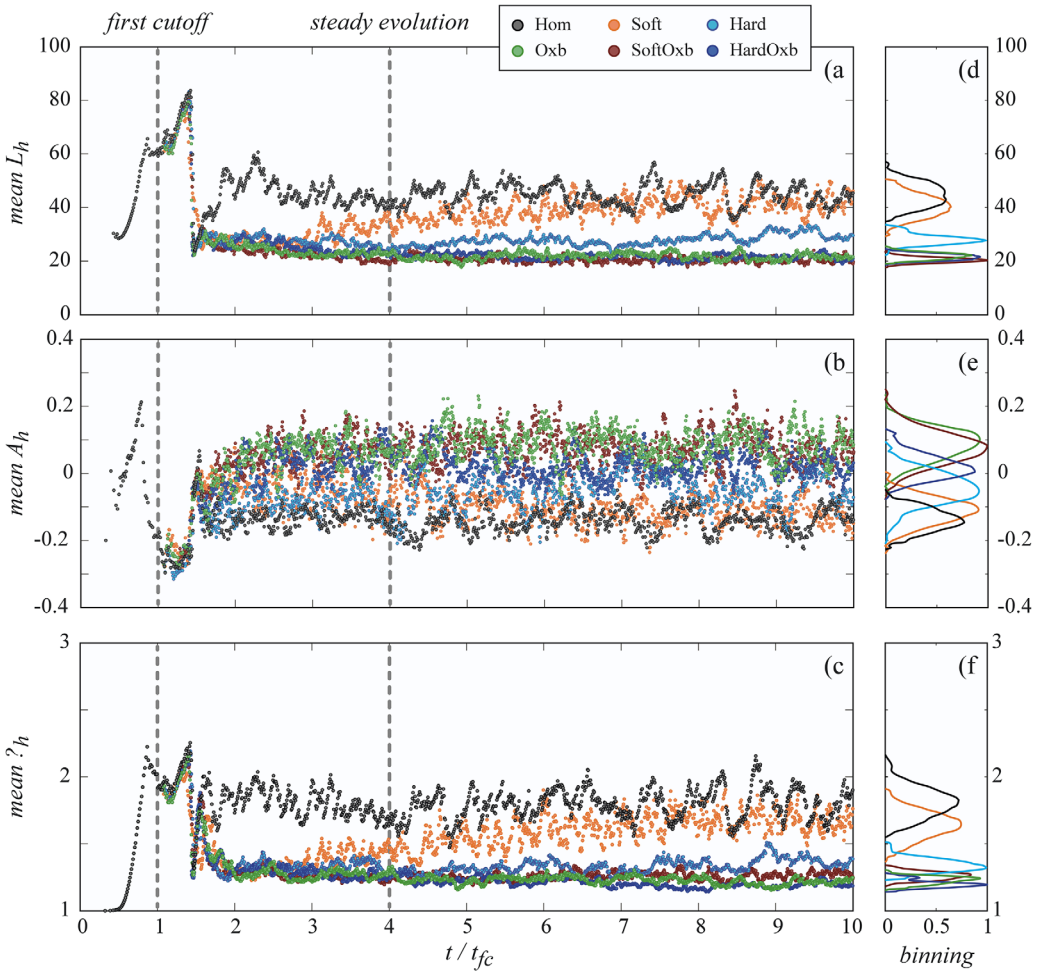

Figure 5. Time evolution of (a) dimensionless half meander length L_h, (b) asymmetry coefficient A_h, and (c) sinuosity σ_h, averaged over the river reach at each time step. Simulations are carried out by considering the six different erodibility scenarios listed in Table 1. Dashed vertical lines correspond to the time t_{fc} of first cutoff and to the time t_{se} ($\sim 4\, t_{fc}$) at which all planform evolutions can be considered statistically stationary. The corresponding frequency distributions of L_h, A_h and σ_h are shown in panels (d), (e) and (f).

assuming either plane or dune covered bed conditions to compute the flow resistance (Table 2). The planforms used in the statistical analyses are extracted randomly from those exhibiting statistically-stationary half meander metrics, i.e., one planform path per run. Simulations are carried out using the ZS fully-coupled morphodynamic model described in section 2 and, for comparison purposes, the uncoupled IPS model.

The results of the test case described in section 3 suggest that introducing different sets of self-formed floodplain heterogeneities leads to different planform shapes both in space and in time. Moreover, al least for the considered set of test parameters, the scenario with hardening scroll bars (H_{ard}) has been found to generate a morphological behaviour that tends to be shifted toward those obtained for less erodible oxbow lakes (O_{xb}, $S_{oft}O_{xb}$, $H_{ard}O_{xb}$). For this reason, and in order to limit the number of simulations, only the effects of scroll bars are accounted for in the simulated path database. The abandoned channel reaches are split in two streamwise regions by the channel axis. The inner half part is considered as belonging to the scroll bar unit, whereas the outer half part is considered as belonging to the surrounding floodplain.

As a consequence, only three different erodibility scenarios are considered for the scroll bar erodibility. The first scenario (*hardening case*) prescribes that the scroll bars are less erodible than the pristine floodplain ($E_b = E_f/8$), as it likely occurs when fine-grained sediments prevails in point bar deposits [*Rowland et al.*, 2005]. The second scenario (*homogeneous case*) consists of geomorphic units that have the same erosion coefficient of the pristine floodplain ($E_b = E_f$). Finally, the third scenario (*softening case*) assumes scroll bars more erodible than the pristine floodplain ($E_b = E_f \times 8$). Differently from the test case discussed in section 3, the differences between E_f and E_b are enhanced to emphasize heterogeneity effects.

Table 2. Sets of Initial Parameters Used in the Numerical Simulations Carried Out to Span Natural-Equivalent Cases[a]

Run	β	τ_*	d_s	Bed Configuration	$(t_{se}/t_{fc})_{ZS}$	$(t_{se}/t_{fc})_{IPS}$
1	10	0.2	0.001	dune-covered	40	10
2	10	0.2	0.01	dune-covered	5	20
3	10	0.7	0.01	plane	2.5	5
4	10	1.2	0.01	plane	4	10
5	15	0.2	0.0001	dune-covered	13	5
6	15	0.2	0.001	dune-covered	10	10
7	15	0.2	0.01	dune-covered	4	50
8	15	0.7	0.001	plane	2	2
9	15	0.7	0.01	plane	4	5
10	15	1.2	0.01	plane	2	10
11	20	0.2	0.0001	dune-covered	3	10
12	20	0.2	0.001	dune-covered	5	30
13	20	0.2	0.01	dune-covered	4	50
14	20	0.7	0.0001	plane	3	2
15	20	0.7	0.001	plane	2	3
16	20	0.7	0.01	plane	1.5	7.5
17	20	1.2	0.001	plane	2	5
18	20	1.2	0.01	plane	1.5	20

[a]Here, β is the half width to depth ratio, τ_* is the Shields number, d_s is the mean sediment size scaled by the flow depth, t_{fc} and t_{se} are the dimensionless time of first cutoff occurrence and the dimensionless time at which statistically-stationary conditions are attained. For a certain set of parameters, t_{se} is determined as the largest value obtained for the three erodibility scenarios (softening, homogeneous, and hardening). The initial bed configuration employed to compute the friction coefficient may be either plane or dune-covered [*Engelund and Hansen*, 1967]. The subscripts ZS and IPS denote the type of model used to carry out the numerical simulations.

For each simulation, the time t_{se} at which the computed planforms attain a statistically-stationary state is determined by analyzing the trends of the three half meander variables L_h, σ_h, and A_h introduced in section 3. Table 2 reports the values of t_{se}/t_{fc} found for the 18 sets of initial parameters. The total simulation time for all runs is at least twice t_{se} to ensure that statistically-stationary evolving conditions are attained. Interestingly, in the present simulations the stationary state is always reached before the pristine floodplain is completely reworked.

4.2. Half Meander Metrics

Figure 6 shows the frequency distribution of half meander metrics L_h, A_h, and σ_h, computed for natural and simulated channel paths. The frequency distribution of L_h in natural rivers decreases as L_h increases, the maximum being close to 100. A similar trend is shown by ZS-generated paths obtained for the hardening scenario, even if some values are larger than 100. Conversely, the softening and the homogeneous ZS-planforms are characterized by much more scattering of the larger values with respect to real rivers, beyond the nonmonotonically decreasing trend. Analogous conclusions may be derived from the frequency distribution of σ_h, even though differences are less pronounced. Finally, plots of A_h distributions reveal that both natural and simulated half meanders exhibit a wide range of skewness. Independently of the considered scenario, IPS-generated paths generally exhibits a wider scatter (especially L_h) and a slightly higher frequency of upstream skewed meanders. In summary, heterogeneities produce variability in terms of half meander length and sinuosity, whereas the asymmetry coefficient does not show any predominant emerging behaviour.

The information provided globally by the half meander metrics can be evaluated by applying the MSSA to the spatial distribution of the three-dimensional signal composed by L_h, A_h, and σ_h, previously normalized via PCA. Figure 7 illustrates the resulting MSSA spectra, and their average values per each component, referred to the different erodibility scenarios. Three windows size are employed to investigate the interplay among adjacent half meanders ($m = 2$) and longer features ($m = 5$ and $m = 8$). The trends suggest qualitatively similar behaviours for all the tested window sizes. In terms of MSSA spectra, the closer similarity with natural geometries is associated with the ZS-generated patterns and the hardening scenario. The similarities are confirmed by the residual sum of squares (RSS) in Figure 7, computed for the simulated average spectra with respect to the natural average spectrum. The progressively larger steepness of the spectra associated with the softening and the homogeneous scenarios points to less structured (i.e., less complex) planform geometries.

4.3. Full Meander Curvature

The spatial distribution of full meander curvature (i.e., defined along reaches delimited by three consecutive inflection points of the channel axis) has been investigated through FA and SSA. Both techniques split the

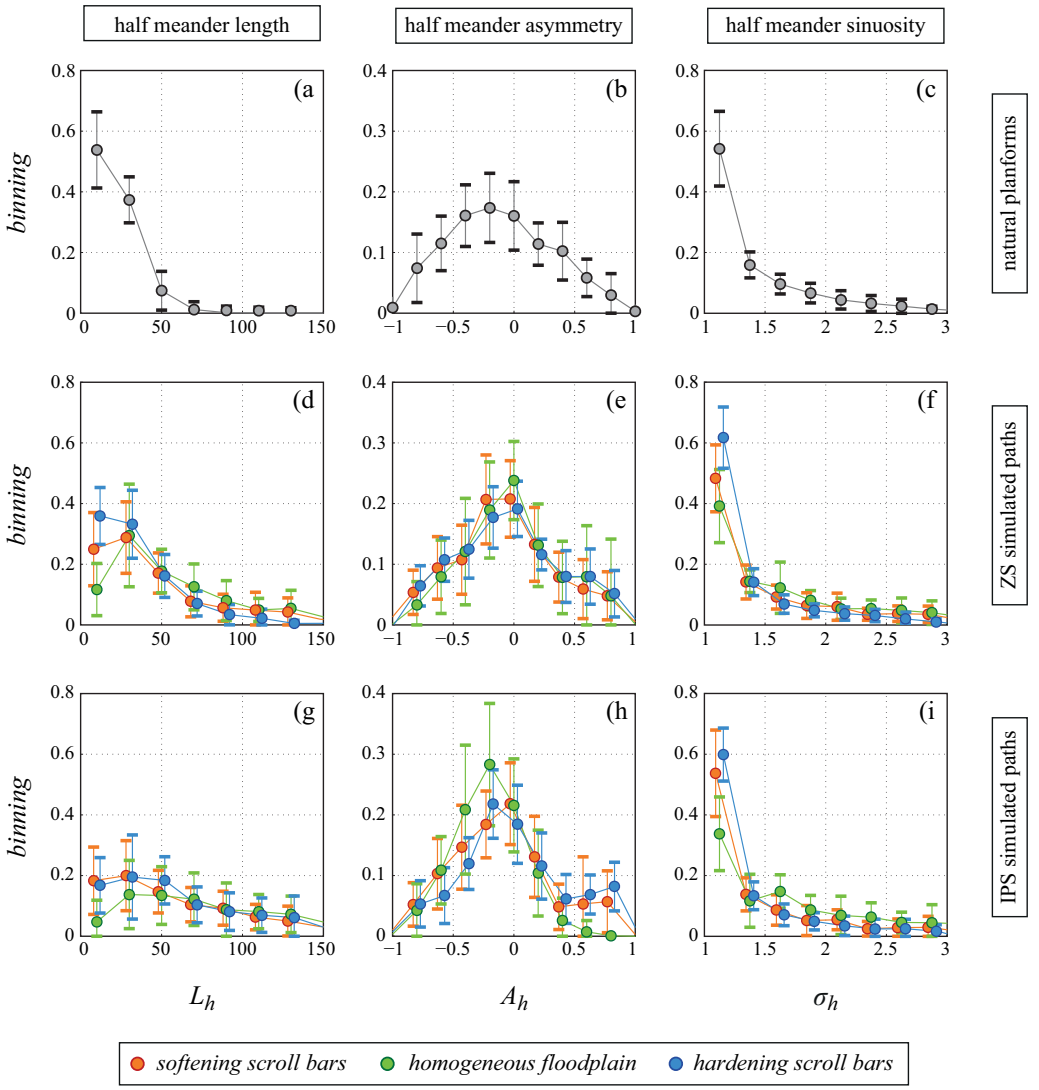

Figure 6. Frequency distributions of spatial series of (a, d, g) dimensionless half meander length L_h, (b, e, h) asymmetry coefficient A_h, and (c, f, i) sinuosity σ_h. (a, b, c) Gray markers refer to natural planforms, while coloured markers refer to either (d, e, f) ZS-simulated paths or (g, h, i) IPS-simulated paths. Vertical bars represent the standard deviations from the average values.

input signal in a set of primitive components, but FA approximates the signal with a series of sinusoidal functions, whereas SSA embeds the input signal in a vector space of given dimension m and projects it on the lag-covariance eigenvectors. Since both natural and simulated full meanders are discretized by polylines, the local curvature $\mathcal{C}_i$ is defined at the ith node of the channel axis, yielding discrete signals.

Figure 8a shows the power spectra, normalized by the power density, of all the considered meanders. The signals are previously detrended, thus the zero harmonics vanish. The first component of the averaged spectra invariably exhibit the highest power, and then the following harmonics decrease monotonically. The average trend most similar to that of natural rivers is attained for the hardening scenario, which slightly overestimates the first and second harmonics and overlaps to the natural trend for the higher harmonics. The average trend of the softening scenarios shows an overestimation of the first harmonic, whereas in the homogeneous case differences with respect to the natural case emerge also in correspondence of the spectra tails. The two flow field models do not produce significantly different spectra.

The information gathered from FA spectra is essentially confirmed by the SSA spectra shown in Figure 8b. In general, all the averaged SSA spectra decay almost exponentially, with a slope break after 3–4 components. Unlike FA spectra, small localized differences emerge not only when considering the various

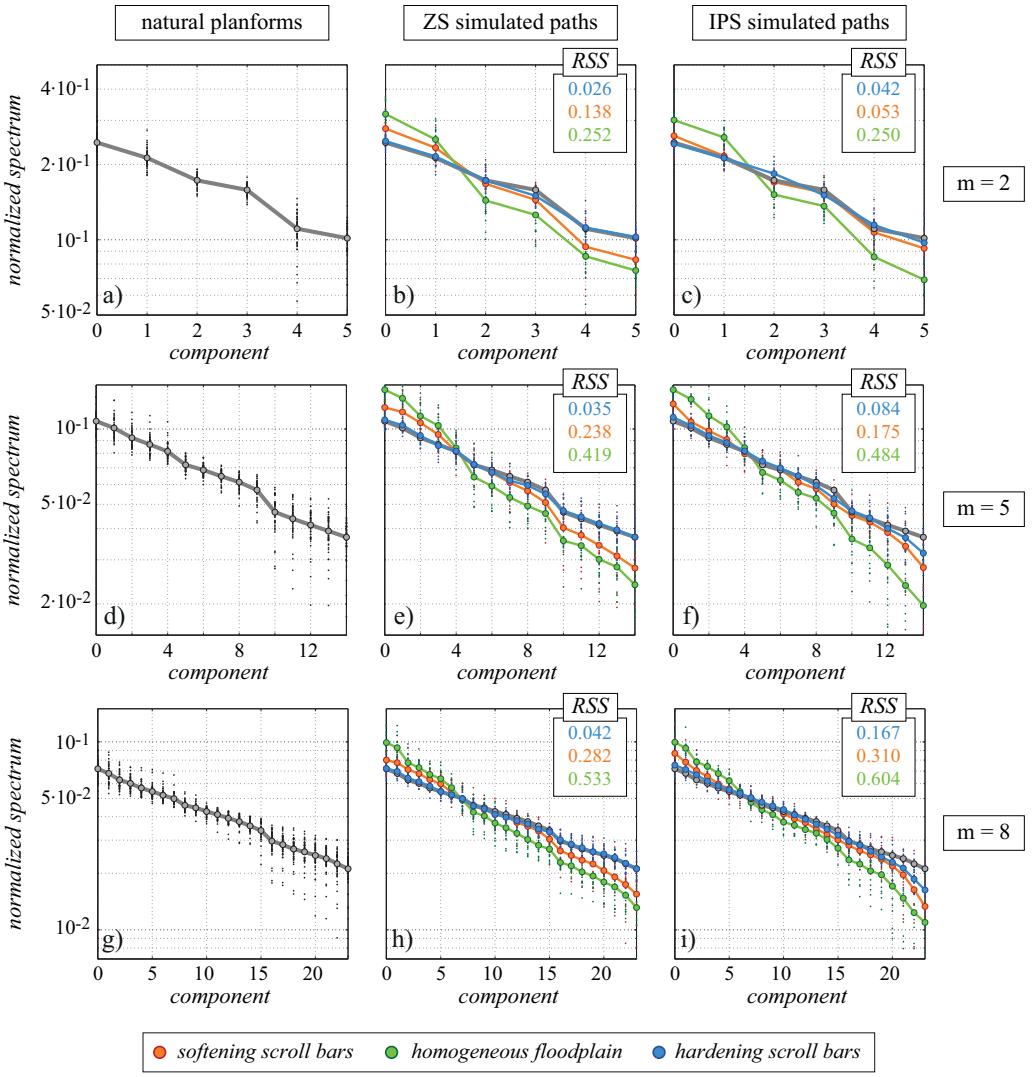

Figure 7. Normalized MSSA spectra of the spatial three-dimensional signals composed by half meander length L_h, half meander asymmetry A_h, and half meander sinuosity σ_h for (a, d, g) natural planforms, (b, e, h) ZS-generated planforms, and (c, f, i) IPS-generated planforms. Three different window sizes are adopted: (a, b, c) $m = 2$, (d, e, f) $m = 5$, and (g, h, i) $m = 8$. The multivariate signals are preprocessed by PCA. Thick lines connect the average values per each spectral component. The average trend of natural paths is repeated in all the other panels for comparison purposes. Values of residual sum of squares (RSS), computed for the simulated average spectra with respect to the natural average spectrum, are coloured on the basis of the average spectrum they refer to.

erodibility scenarios, but also when using different flow field models. In particular, the major differences between natural and simulated paths are observed for the homogeneous scenarios, where the second and third components are generally lower than that of the natural case, especially for IPS-simulated paths. In the presence of heterogeneities, the spectra associated with ZS-generated patterns exhibit a diffuse shift of the mean trend with respect to natural paths, but the differences keep rather limited.

In summary, FA and SSA analyses of meander curvature suggest that introducing any kind of self-formed heterogeneity on the floodplain leads to relatively similar averaged spectra, with minor differences with respect to natural patterns. The analyses of full meander curvature thus seem to poorly discriminate between different planforms, in accordance with the findings of *Frascati and Lanzoni* [2009].

4.4. Overall Spatial Comparison

The results described in sections 4.2 and 4.3 indicate that many variables are needed to fully describe the variety of meandering patterns. Following the approach of *Frascati and Lanzoni* [2009], a suite of

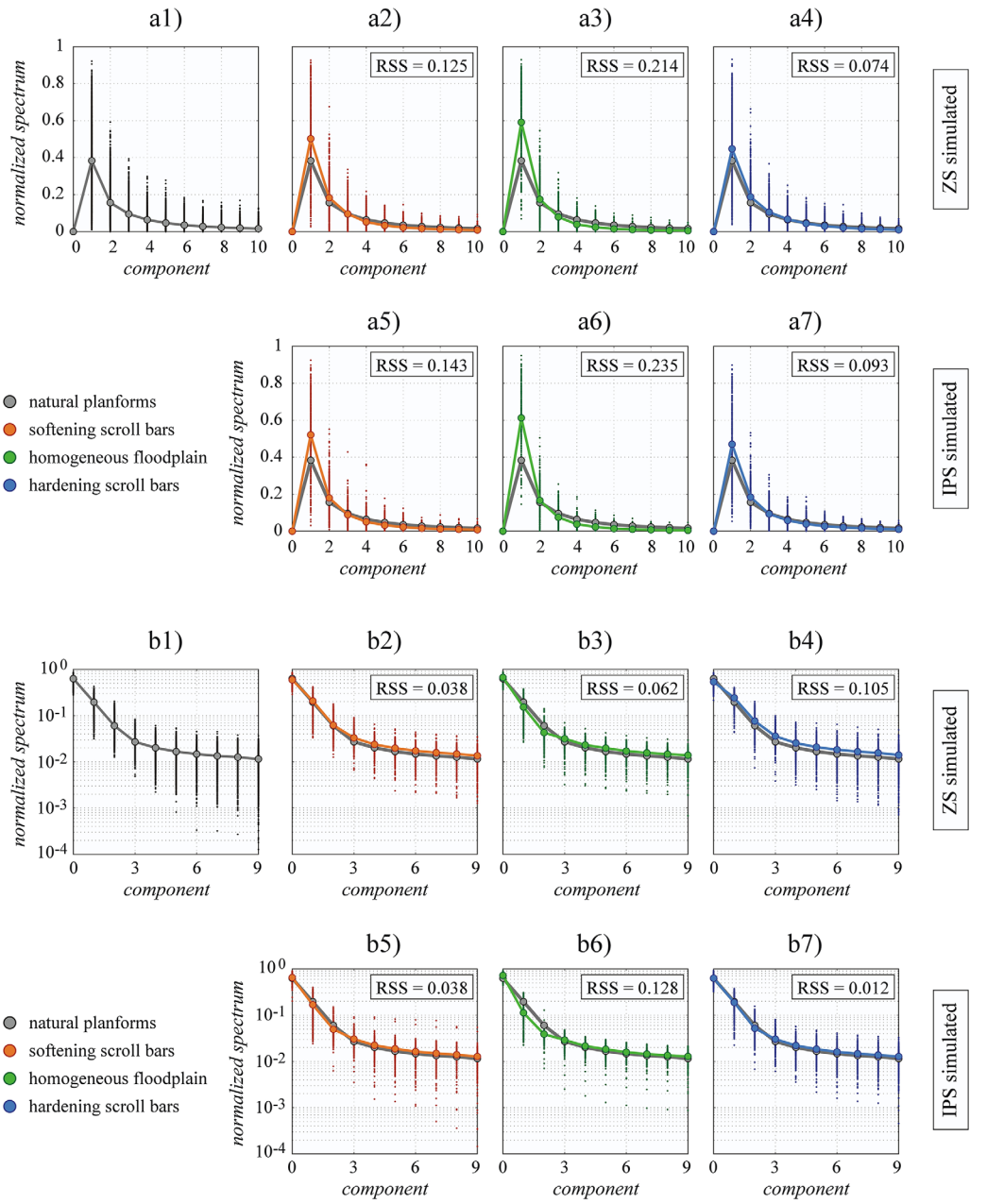

Figure 8. Normalized spectra of the full meander curvature. (a) FA power spectra of spatial distributions of full meander curvature, normalized to the total power density, for natural planforms (a1), ZS-simulated paths (a2,a3,a4), and IPS-simulated paths (a5,a6,a7). (b) Normalized SSA spectra of spatial distributions of full meander curvature, for natural planforms (b1), ZS-simulated paths (b2,b3,b4), and IPS-simulated paths (b5,b6,b7), for a window size $m = 10$. Solid lines connect the average values per harmonic. The average trend of natural paths is repeated in all the other panels for comparison purposes. Values of residual sum of squares (RSS) are computed for the simulated average spectra with respect to the natural average spectrum.

16 morphometric variables (supporting information Table S1) is then introduced to characterize, through Principal Component Analysis (PCA), the complexity embedded in meandering geometries and to emphasize the subtle differences which may emerge between apparently similar configurations. The set includes quantities related to three different scales: half meander, full meander and whole reach. At the half meander scale, the considered quantities are the mean, the variance, the skewness and the kurtosis of the along channel distributions of L_h, A_h and σ_h. The full meander scale (denoted with the subscript f) is represented by the spatially-averaged sinuosity:

$$\sigma_{f,mean} = \frac{1}{N_f}\sum_{i=1}^{N_f}\frac{L_{fi}}{l_{fi}} \tag{17}$$

where L_f and l_f are the intrinsic and the Cartesian lengths of the full meander, normalized by B_0^*, while N_f is the number of full meanders forming the reach. Further quantities referring to the full meander scale (e.g., asymmetry) are redundant with respect to the half meander quantities. Finally, the reach scale (denoted with the subscript t) is accounted for through the variance and kurtosis of the distribution of local curvature, and through the reach sinuosity:

$$\sigma_t = \frac{L_t}{l_t} \tag{18}$$

where L_t and l_t are the intrinsic and Cartesian lengths of the reach, normalized by B_0^*.

The PCA is performed on the matrix that results by assembling the row vectors containing the above defined 16 statistical variables for each path. The aim is to convert the original data set in an equivalent data set with a lower dimensionality, but ensuring a relatively small loss of information. Figure 9 shows the three-dimensional scatter plot of the first three components relative to the three largest eigenvalues, together with the two-dimensional projections of the resulting combinations of pairs. The first three components a_1, a_2, a_3 account for about 55% of the total variance. The spatial distribution is relatively significant, with a clear separation of the homogeneous scenario markers, which are more spread (in particular for IPS-simulated paths), and the natural planform markers, which tends to be clustered. Softening case and hardening case markers lie between the previous two sets, with the latter partially overlapping the natural path cluster, in particular for ZS-simulated paths. The first two PCA components, a_1 and a_2, account for about 45% of the total variance. The clustering of the softening scenario markers is evident, as well as the proximity of the hardening scenario markers to those characterizing natural paths, which are mainly concentrated in the quadrant where a_1 is positive and a_2 is negative. The markers corresponding to the homogeneous case are very spread, and mainly localized in the negative a_1 half-plane, thus showing an opposite behaviour with respect to the natural path cluster.

The degree of clustering decreases with the order of the components, as the total variance accounted for by the components and the difference in variance between two consecutive components progressively decrease. While in the a_1 - a_3 plane the clustering clearly emerges, in the a_2 - a_3 plane only the natural path cluster remains relatively clear. Indeed, the normalized PCA spectrum is an indicator of the splitting of information along the Principal Components, analogously to SSA, MSSA and FA. The PCA spectrum decays nearly exponentially (i.e., linearly in the semi-log plot) up to small values of the order of 10^{-3}, with the successive 13 out of 16 eigenvalues carrying the residual variance (about 45%), not described by the first three components.

The results confirm the closer affinity with natural planforms displayed by numerically generated meanders in the presence of less erodible scroll bars.

5. Discussion

Outer bank erosion, point bar accretion, fine-grained fills of abandoned channels, sedimentation during over-bank floods and spilling of tie and tributary channels, crevasse splay through levee breaches, organic-reach backswamp deposits, and vegetation encroachment are some of the processes that concur to shape the lowland floodplain environment. The numerical study of their mutual interactions and feedbacks requires a modeling effort that is still ongoing. Even though many advanced physics-based morphodynamic models are currently available, for long-term time scales we still need to resort to a simplified description of the relevant processes in order to gain a better understanding of how nature works and to provide a robust observational underpinning. For these reasons, we focused our attention only on two of the many geomorphic structures built up by river migration that contribute to control the sedimentary architecture of a floodplain, namely scroll bars and oxbow lakes.

The hardening scenario can be considered as representative of erosion resistant oxbow fills and counter point bar deposits in rivers with high enough fine sediment loads, possibly reinforced by vegetation growth. Conversely, the softening scenario can be related to the case of sandy point bars deposits and oxbow lakes

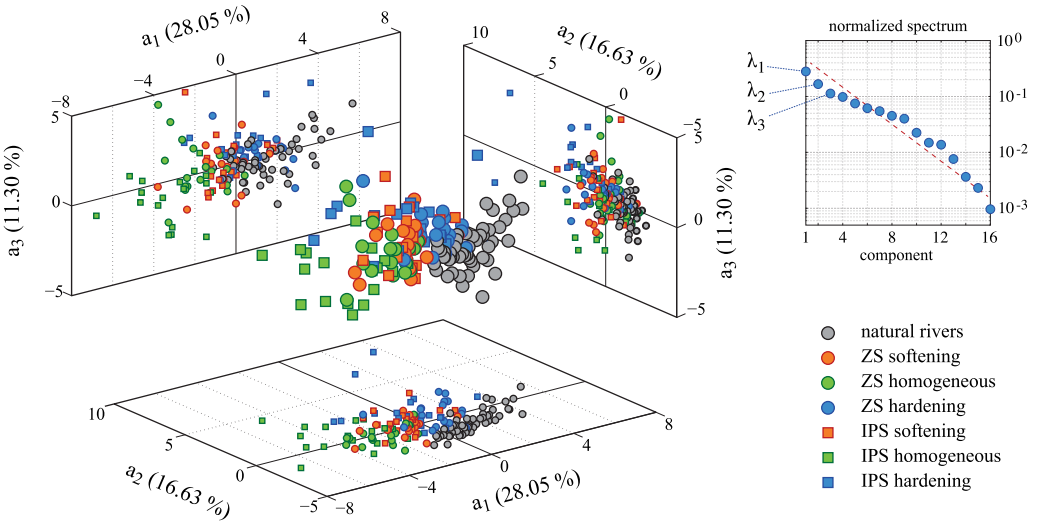

Figure 9. Three-dimensional scatter plot of the first three PCA components resulting from the analysis of the morphometric variables listed in section 4.4 (see supporting information Table S1), and concerning natural rivers and simulated paths. The lateral panels show the orthogonal projections on the planes (a_1, a_2), (a_1, a_3) and (a_2, a_3). Each axis reports the respective percentage of variance. The panel on the top right corner shows the eigenvalue spectrum, normalized with the total density.

that either exist as open water bodies for many decades, owing to a relatively low supply of sediment, or are intercepted soon after their formation in highly active rivers, with rapid migration and large cutoff rates. Present results show that the heterogeneity in floodplain composition associated with the formation of preserved geomorphic units and the choice of a reliable flow field model to drive channel migration are two fundamental ingredients for reproducing correctly the long-term morphodynamics of alluvial meanders.

After a statistically steady state is attained by the river evolution, the frequency distribution of half meander metrics (especially length and sinuosity) is found to depend on the erosional strength associated with floodplain heterogeneities. From a purely geometrical point of view, all morphological analyses of spatial features concur to establish that patterns generated by assuming the scroll bar environments less erodible than the surrounding floodplain are more akin to the considered natural meander shapes. More specifically, the normalized MSSA spectra of the spatial distributions of half meander metrics indicate that assuming a hardening scenario (less erodible oxbow lakes and point bars) leads to less sloping spectra tails and, consequently, to more complex (more structured) planforms with respect to the homogeneous and softening scenarios. The FA and SSA analyses applied to spatial distribution of local channel axis curvature suggest that the averaged spectra are quite similar and only minor differences are found when considering the different erosional scenarios. Conversely, the overall spatial comparison carried out by applying PCA to statistics involving meander length, asymmetry, sinuosity, and curvature, reveals the differences among planform configurations obtained for the various erosional scenarios and, in particular, the closer similarity with natural meanders that results when assuming less erodible self-formed heterogeneities.

Moreover, even in the presence of river-induced floodplain heterogeneities, patterns generated by using a fully-coupled hydro-morphodynamic flow field model (as the ZS one) are still those that better resemble natural landforms [*Frascati and Lanzoni*, 2009]. This result stresses the importance to use a morphodynamic model that accounts for the whole range of morphodynamic conditions (sub-resonant and super-resonant) and, hence, is in any case able to reproduce the wide variety of bends (upstream-skewed, downstream-skewed, compound, multiple loops) observed in nature.

Clearly, other processes can affect the distribution of heterogeneities across a floodplain, and deserve attention in future research. Oxbow lakes created by chute cutoffs (not treated in the present simulations) generally have lower diversion angles than neck cutoffs. The enhanced delivery of coarse sediment from the active channel thus tends to slow the closure of the abandoned reach [*Constantine et al.*, 2010], with a consequently modified (likely smaller) resistance to erosion when the active meandering river migrate again into the oxbow. Geological constraint (e.g., rock outcrops), land use, and vegetation patterns matter as well. In many cases, woodland species are densest along the boundaries of the active river and oxbow lakes, while grassland species prevail

on the remaining floodplain. The high density of large roots in cutbanks thus decreases bank erodibility [*Allmendinger et al.*, 2005]. Nevertheless, when vegetation is confined to the tops of tall cutbanks, the erosion at the toe of the bank eventually undermines even root-reinforced slopes [*Constantine et al.*, 2009]. These eco-morphodynamic processes need to be included in long-term models of alluvial river evolution.

6. Conclusions

The aim of this work is to investigate the mutual interactions between a meandering river and the adjacent floodplain as the sedimentary structure of the alluvial surface is reworked by the river itself. Floodplain destruction is caused by meander bend migration consequent to the outer bank collapse. Floodplain reconstruction is related to lateral point bar accretion at the inner bank. In the modeling framework, self-formed floodplain heterogeneities are associated to the formation of scroll bars, resulting in a typical ridge-and-swale sequence, and oxbow lake fills. The main conclusions of our analysis can be summarized as follows.

The long-term evolution of meandering rivers turns out to be significantly influenced by self-formed floodplain heterogeneities. They are found to affect both the temporal and spatial distributions of meander metrics, eventually leading to a closer statistical similarity between simulated and natural planform shapes. A flow field model fully coupled with the bed evolution equation, and hence able to describe the full ranges of morphological regimes (sub-resonant and super-resonant), is found to better reproduce natural planforms even in the presence of self-formed floodplain heterogeneities. Planform complexity is generated by meander elongation through bend erosion and the interplay of heterogeneities in bank strength. Conversely, removal of older, more developed meanders by cutoff processes tends to reduce this complexity. The signature of the morphological regime (either sub-resonant or super-resonant) contributes to further characterize planform geometry.

Statistical and spectral analyses (Fourier Analysis, Singular Spectrum Analysis, Multivariate Singular Spectrum Analysis, and Principal Component Analysis) prove to be useful tools for a quantitative description of the complexity embedded in meander shapes. Assuming less erodible oxbow lakes and point bars (hardening scenario) leads to more complex (more structured) planforms with respect to the homogeneous and softening scenarios. Spatial distribution of local channel axis curvature, by itself, is not sufficient to fully characterize the subtle but fundamental differences among planforms paths. These differences are instead evident when PCA is applied to a selected set of morphodynamics variables, spanning half meander, full meander and whole reach scales. This methodology, indeed, facilitates the identification of the differences that mostly contribute to the deviations among signals coming from the various data sets.

Within the range of natural-equivalent cases considered in the parameter space, the closer affinity with natural planforms is invariably displayed by numerically generated meanders in the presence of self-formed floodplains units that are less erodible than the surrounding floodplain.

Acknowledgments
The authors thank M. G. Kleinhans and the two other anonymous reviewers for the useful suggestions and inspiring comments that helped to significantly improve the manuscript. Data for this paper are properly cited and referred to in the reference list. Supporting data and methods are included in an SI file; any additional data may be obtained from MB (email: manuel.bogoni@dicea.unipd.it). The source code for the model used in this study is available at github.com/FluidMechanicsUNIPD.

References

Aalto, R. E., J. W. Lauer, and W. E. Dietrich (2008), Spatial and temporal dynamics of sediment accumulation and exchange along Strickland River floodplains (Papua New Guinea) over decadal-to-centennial timescales, *J. Geophys. Res.*, *113*, F01S04, doi:10.1029/2006JF000627.

Allmendinger, N. E., J. E. Pizzuto, N. Potter, T. E. Johnson, and W. C. Hession (2005), The influence of riparian vegetation on stream width, eastern Pennsylvania, USA, *Bull. Geol. Soc. Am.*, *117*(1-2), 229–243.

Asahi, K., Y. Shimizu, J. Nelson, and G. Parker (2013), Numerical simulation of river meandering with self-evolving banks, *J. Geophys. Res. Earth Surf.*, *118*, 2208–2229, doi:10.1002/jgrf.20150.

Blondeaux, P., and G. Seminara (1985), A unified bar-bend theory of river meanders, *J. Fluid Mech.*, *157*, 449–470.

Bolla Pittaluga, M., and G. Seminara (2011), Nonlinearity and unsteadiness in rivermeandering: A review of progress in theory and modelling, *Earth Surf. Processes Landforms*, *36*(1), 2038, doi:10.1002/esp.2089.

Browlie, W. R. (1981), Re-examination of Nikuradse roughness data, *J. Hydraulic Div. Am. Soc. Civ. Eng.*, *107*(HY1), 115–119.

Camporeale, C., P. Perona, A. Porporato, and L. Ridolfi (2005), On the long-term behavior of meandering rivers, *Water Resour. Res.*, *41*, W12403, doi:10.1029/2005WR004109.

Camporeale, C., E. Perucca, and L. Ridolfi (2008), Significance of cutoff in meandering river dynamics, *J. Geophys. Res.*, *113*, F01001, doi:10.1029/2006JF000694.

Constantine, C. R., T. Dunne, and G. J. Hanson (2009), Examining the physical meaning of the bank erosion coefficient used in meander migration modeling, *Geomorphology*, *106*(3–4), 242–252.

Constantine, J. A., T. Dunne, H. Piégay, and G. Mathias Kondolf (2010), Controls on the alluviation of oxbow lakes by bed-material load along the Sacramento river, California, *Sedimentology*, *57*(2), 389–407.

Crosato, A. (1990), Simulation of meandering river process, *Commun. Hydraul. Geotech. Eng.*, *90*(3), 109.

David, S. R., D. A. Edmonds, and S. Letsinger (2016), Controls on the occurrence and prevalence of floodplain channels in meandering rivers, *Earth Surf. Processes Landforms*, *42*(3), 460–472.
Day, G., W. E. Dietrich, J. C. Rowland, and A. Marshall (2008), The depositional web on the floodplain of the Fly River, Papua New Guinea, *J. Geophys. Res.*, *113*, F01S02, doi:10.1029/2006JF000622.
Dunne, T., L. Mertes, R. Meade, J. Richey, and B. Forsberg (1998), Exchanges of sediment between the floodplain and channel of the Amazon River in Brazil, *Geol. Soc. Am. Bull.*, *110*(4), 450–467.
Eke, E. C., G. Parker, and Y. Shimizu (2014), Numerical modeling of erosional and depositional bank processes in migrating river bends with self-formed width: Morphodynamics of barp ush and bank pull, *J. Geophys. Res. Earth Surf.*, *119*(7), 1455–1483.
Engelund, F., and E. Hansen (1967), A monograph on sediment transport in alluvial stream, technical report, TEKNISKFORLAG Skelbrekgade 4 Copenhagen V, Denmark.
Ferguson, R. (1987), Hydraulic and sedimentary controls of channel pattern, in *River Channels: Environment and Process, Inst. of Br. Geogr. Spec. Publ*. 18, edited by K. Richards, pp. 129–158, Blackwell, Oxford, U. K.
Frascati, A., and S. Lanzoni (2009), Morphodynamic regime and long-term evolution of meandering rivers, *J. Geophys. Res.*, *114*, F02002, doi:10.1029/2008JF001101.
Frascati, A., and S. Lanzoni (2010), Long-term river meandering as a part of chaotic dynamics? A contribution from mathematical modelling, *Earth Surf. Processes Landforms*, *35*(7), 791–802.
Frascati, A., and S. Lanzoni (2013), A mathematical model for meandering rivers with varying width, *J. Geophys. Res. Earth Surf.*, *118*, 1641–1657, doi:10.1002/jgrf.20084.
Gagliano, S. M., and P. C. Howard (1984), The neck cutoff oxbow lake cycle along the Lower Mississippi River, in *Proceedings of the Conference Rivers 1983 on River Meandering*, edited by E. CM, pp. 147–158, ASCE New Orleans, La.
Gautier, E., D. Brunstein, P. Vauchel, M. Rouler, O. Fuertes, L. Guyot, J. Darozzes, and L. Bourrel (2007), Temporal relation between meander deformation, water discahrge and sediment fluxes in the floodplain of the Rio Beni (Bolivian Amazonia), *Earth Surf. Processes Landforms*, *32*, 230–248.
Gay, G. R., H. H. Gay, W. H. Gay, H. A. Martinson, R. H. Meade, and J. A. Moody (1998), Evolution of cutoffs across meander nechks in Powder River, Montana, USA, *Earth Surf. Processes Landforms*, *23*, 651–662.
Ghil, M., et al. (2002), Advanced spectral methods for climate time series, *Rev. Geophys.*, *40*(1), 1003, doi:10.1029/2000RG000092.
Grenfell, M., R. E. Aalto, and A. P. Nicholas (2012), Chute channel dynamics in large, sand-bed meandering rivers, *Earth Surf. Processes Landforms*, *37*(3), 315–331.
Güneralp, Í., and B. L. Rhoads (2011), Influence of floodplain erosional heterogeneity on planform complexity of meandering rivers, *Geophys. Res. Lett.*, *38*, L14401, doi:10.1029/2011GL048134.
Han, B., and T. Endreny (2014), Detailed river stage mapping and head gradient analysis during meander cutoff in a laboratory river, *Water Resour. Res.*, *50*, 1689–1703, doi:10.1002/2013WR013580.
Hooke, J. M. (1995), River channel adjustment to meander cutoffs on the river Bollin and river Dane, northwest England, *Geomorphology*, *14*, 235–253.
Hooke, J. M. (2004), Cutoffs galore!: Occurrence and causes of multiple cutoffs on a meandering river, *Geomorphology*, *61*(3–4), 225–238.
Hormann, K., and A. Agathos (2001), The point in polygon problem for arbitrary polygons, *Comput. Geometry Theory Appl.*, *20*(3), 131–144.
Howard, A. (1996), Modelling channel migration and floodplain development in meandering streams, *Lowland Floodplain Rivers: Geomorphological Perspectives*, edited by P. A. Carling and G. E. Petts, pp. 2–41, John Wiley, New York.
Howard, A. D., and A. T. Hemberger (1991), Multivariate characterization of meandering, *Geomorphology*, *4*, 161–186.
Howard, A. D., and T. R. Knutson (1984), Sufficient conditions for river meanering: A simulation approach, *Water Resour. Res.*, *20*(11), 1659–1667.
Hudson, P. F., and R. H. Kesel (2000), Channel migration and meander-bend curvature in the lower Mississippi River prior to major human modification, *Geology*, *28*(6), 531–534.
Ikeda, S., G. Parker, and K. Sawai (1981), Bend theory of river meanders: Part 1: Linear development, *J. Fluid Mech.*, *112*, 363–377.
Johannesson, H., and G. Parker (1989), Linear theory of river meanders, *Water Resour. Monogr.*, *12*, 181–214.
Kleinhans, M. G. (2010), Sorting out river channel patterns, *Prog. Phys. Geogr.*, 3(*34*), 287–326.
Lancaster, S. T., and R. L. Bras (2002), A simple model of river meandering and its comparison to natural channels, *Hydrol. Processes*, *16*(1), 1–26.
Lane, E. W. (1957), *A Study of the Shape of Channels Formed by Natural Streams Flowing in Erodible Material*, U.S. Army Eng. Div, Missouri River.
Lanzoni, S., and G. Seminara (2006), On the nature of meander instability, *J. Geophys. Res.*, *111*, F04006, doi:10.1029/2005JF000416.
Lanzoni, S., A. Siviglia, A. Frascati, and G. Seminara (2006), Long waves in erodible channels and morphodynamic influence, *Water Resour. Res.*, *42*, W06D17, doi:10.1029/2006WR004916.
Latrubesse, E. M. (2008), Patterns of anabranching channels: The ultimate end-member adjustment of mega rivers, *Geomorphology*, *101*(1–2), 130–145.
Lauer, J. W., and G. Parker (2008), Net local removal of floodplain sediment by river meander migration, *Geomorphology*, *96*(1–2), 123–149.
Lazarus, E. D., and J. A. Constantine (2013), Generic theory for channel sinuosity, *Proc. Natl. Acad. Sci. U. S. A.*, *110*(21), 8447–8452.
Leopold, L. B., and M. G. Wolman (1957), *River Channel Patterns: Braided, Meandering, and Straight*, U.S. Gov. Print. Off., Washington, D. C.
Makaske, B. (2001), Anastomosing rivers: A review of their classification, origin and sedimentary products, *Earth Sci. Rev.*, *53*, 149–196.
Makaske, B., D. G. Smith, and H. J. A. Berendsen (2002), Avulsions, channel evolution and floodplain sedimentation rates of the anastomosing upper Columbia River, British Columbia, Canada, *Sedimentology*, *49*(5), 1049–1071.
Marani, M., S. Lanzoni, and D. Zandolin (2002), Tidal meanders, *Water Resour. Res.*, *38*(11), 1225, doi:10.1029/2001WR000404.
Motta, D., J. D. Abad, E. J. Langendoen, and M. H. Garcia (2012a), A simplified 2D model for meander migration with physically-based bank evolution, *Geomorphology*, *163*, 10–25.
Motta, D., J. D. Abad, E. J. Langendoen, and M. H. Garcia (2012b), The effects of floodplain soil heterogeneity on meander planform shape, *Water Resour. Res.*, *48*, W09518, doi:10.1029/2011WR011601.
Nanson, G. C. (1980), Point bar and floodplain formation of the meandering Beatton River, Northeastern British Columbia, Canada, *Sedimentology*, *27*(1), 3–290
Nanson, G. C., and J. C. Croke (1992), A genetic classification of floodplains, *Geomorphology*, *4*, 459–486.
Nicoll, T.J., and E. J. Hickin (2010), Planform geometry and channel migration of confined meandering rivers on the Canadian prairies, *Geomorphology*, *116*(1–2), 37–47.
Orfanidis, S. J. (1995), *Introduction to Signal Processing*, Prentice Hall, Upper Saddle River, N. J.
Parker, G. (1976), On the cause and characteristic scales of meandering and braiding in rivers, *J. Fluid Mech.*, *76*(3), 457–480.

Parker, G. (1990), Surface-based bedload transport relation for gravel rivers, *J. Hydraul. Res.*, *28*(4), 417–436.
Parker, G., Y. Shimizu, G. V. Wilkerson, E. C. Eke, J. D. Abad, J. W. Lauer, C. Paola, W. E. Dietrich, and V. R. Voller (2011), A new framework for modeling the migration of meandering rivers, *Earth Surf. Processes Landforms*, *36*(1), 70–86.
Perucca, E., C. Camporeale, and L. Ridolfi (2005), Nonlinear analysis of the geometry of meandering rivers, *Geophys. Res. Lett.*, *32*, L03402, doi:10.1029/2004GL021966.
Perucca, E., C. Camporeale, and L. Ridolfi (2006), Influence of river meandering dynamics on riparian vegetation pattern formation, *J. Geophys. Res.*, *111*, G01001, doi:10.1029/2005JG000073.
Perucca, E., C. Camporeale, and L. Ridolfi (2007), Significance of the riparian vegetation dynamics on meandering river morphodynamics, *Water Resour. Res.*, *43*, W03430, doi:10.1029/2006WR005234.
Rowland, J. C., K. Lepper, W. E. Dietrich, C. J. Wilson, and R. Sheldon (2005), Tie channel sedimentation rates, oxbow formation age and channel migration rate from optically stimulated luminescence (OSL) analysis of floodplain deposits, *Earth Surf. Processes Landforms*, *30*(9), 1161–1179.
Schumm, S. A. (1985), Patterns of alluvial rivers, *Annu. Rev. Earth Planet. Sci.*, *13*, 527.
Schumm, S. A. (1986), Alluvial river response to active tectonics, in *Active Tectonics*, pp. 80–94, National Academy Press, Washington, D. C.
Schuurman, F., Y. Shimizu, T. Iwasaki, and M. G. Kleinhans (2016), Dynamic meandering in response to upstream perturbations and floodplain formation, *Geomorphology*, *253*, 94–109.
Schwenk, J., S. Lanzoni, and E. Foufoula-Georgiou (2015), The life of a meander bend: Connecting shape and dynamics via analysis of a numerical model, *J. Geophys. Res. Earth Surf.*, *120*, 690–710, doi:10.1002/2014JF003252.
Seminara, G. (2006), Meanders, *J. Fluid Mech.*, *554*, 271–297.
Seminara, G., G. Zolezzi, M. Tubino, and D. Zardi (2001), Downstream and upstream influence in river meandering: Part 2. Planimetric development, *J. Fluid Mech.*, *438*, 213–230.
Serita, A., K. Hattori, C. Yoshino, M. Hayakawa, and N. Isezaki (2005), Principal component analysis and singular spectrum analysis of ULF geomagnetic data associated with earthquakes, *Nat. Hazards Earth Syst. Sci.*, *5*(5), 685–689.
Slingerland, R., and N. D. Smith (2004), River avulsions and their deposits, *Annu. Rev. Earth Planet. Sci.*, *32*(Qian 1990), 257–285.
Smith, D. G., S. M. Hubbard, D. A. Leckie, and M. Fustic (2009), Counter point bar deposits: Lithofacies and reservoir significance in the meandering modern peace river and ancient McMurray formation, Alberta, Canada, *Sedimentology*, *56*(6), 1655–1669.
Solari, L., van Oorschot, M., Belletti, B., Hendriks, D., Rinaldi, M., and A. Vargas-Luna (2016), Advances on modelling riparian vegetation - hydromorphology interactions, *River Res. Appl.*, *32*, 164–178.
Sun, T., P. Meakin, T. Jø ssang, and K. Schwarz (1996), A simulation model for meandering rivers, *Water Resour. Res.*, *32*(9), 2937–2954, doi: 10.1029/96WR00998.
Swanson, K. M., E. Watson, R. E. Aalto, J. W. Lauer, M. T. Bera, A. Marshall, M. P. Taylor, S. C. Apte, and W. E. Dietrich (2008), Sediment load and floodplain deposition rates: Comparison of the Fly and Strickland rivers, Papua New Guinea, *J. Geophys. Res. Earth Surf.*, *113*, F01S03, doi:10.1029/2006JF000623.
Toonen, W. H. J., M. G. Kleinhans, and K. M. Cohen (2012), Sedimentary architecture of abandoned channel fills, *Earth Surf. Processes Landforms*, *47*(4), 459–472.
van de Lageweg, W. I., W. M. van Dijk, A. W. Baar, J. Rutten, and M. G. Kleinhans (2014), Bank pull or bar push: What drives scroll-bar formation in meandering rivers?, *Geology*, *42*(4), 319–322.
Van den Berg, J. H. (1995), Prediction of alluvial channel pattern of perennial rivers, *Geomorphology*, *12*(4), 259–279.
van Oorschot, M., M. G. Kleinhans, G. Geerling, and H. Middelkoop (2016), Distinct patterns of interaction between vegetation and morphodynamics, *Earth Surf. Processes Landforms*, *41*(6), 791–808.
Van Rijn, L. C. (1984a), Sediment transport, part II: Suspended load transport, *J. Hydraul. Eng.*, *110*(11), 1613–1641.
Van Rijn, L. C. (1984b), Sediment transport, part III: Bed forms and alluvial roughness, *J. Hydraul. Eng.*, *110*(12), 1733–1754.
Vautard, R., and M. Ghil (1989), Singular spectrum analysis in nonlinear dynamics with applications to paleoclimatic time series, *Physica D*, *35*, 395–424.
Wickert, A. D., J. M. Martin, M. Tal, W. Kim, B. Sheets, and C. Paola (2013), River channel lateral mobility: Metrics, time scales, and controls, *J. Geophys. Res. Earth Surf.*, *118*, 396–412, doi:10.1029/2012JF002386.
Zen, S., Zolezzi, G., M. Toffolon, and A. M. Gurnell (2016), Biomorphodynamic modelling of inner bank advance in migrating meander bends, *Adv. Water Resour.*, *93*, 166–181.
Zolezzi, G., and G. Seminara (2001), Downstream and upstream influence in river meandering: Part 1. General theory and application to overdeepening, *J. Fluid Mech.*, *438*, 183–211.